JOURNAL OF THERMOPHYSICS AND HEAT TRANSFER
Vol. 26, No. 1, January–March 2012

Coupled DSMC—PMC Radiation Simulations of a Hypersonic Reentry

I. Sohn,* Z. Li,† and D. A. Levin‡
Pennsylvania State University, University Park, Pennsylvania 16801
and
M. F. Modest§
University of California, Merced, Merced, California 95343

DOI: 10.2514/1.T3633

During extreme-Mach-number reentry into Earth's atmosphere, spacecraft experience hypersonic nonequilibrium flow conditions that dissociate molecules and ionize atoms. Since the electronic levels of atomic species are strongly excited for high-Mach-number conditions, the radiative contribution to the total heat load can be significant. To perform accurate and efficient analyses of chemically reacting flowfield—radiation interactions, the direct simulation Monte Carlo (DSMC) and the photon Monte Carlo (PMC) radiative transport methods are used to simulate flowfield—radiation coupling from transitional to peak heating freestream conditions. The first DSMC—finite-volume PMC simulations are presented with the goal of understanding the effect of radiation on the flow structure for different degrees of hypersonic nonequilibrium. It is found that, except for the highest altitudes, the coupling of radiation influences the flowfield, leading to a decrease in both heavy particle translational and internal temperatures and a decrease in the convective heat flux to the body. The DSMC—PMC coupled simulations are compared with the previous coupled simulations and correlations obtained using continuum flow modeling and one-dimensional radiative transport. The DSMC simulations are also extended to consider the effect of gas-surface interactions on the convective heat flux.

Nomenclature

b_{hw}	=	line half-width, Å
E	=	radiative energy, W
E_{abs}	=	radiative energy absorbed by cell, W
E_{bundle}	=	radiative energy carried by photon bundle, W
E_{emis}	=	emission energy, W
E_{trans}	=	transmitted radiative energy, W
$K_{n,\infty}$	=	freestream Knudsen number, dimensionless
k, k_1, k_2	=	line-center index, dimensionless
L	=	nose radius of the Stardust blunt body, m
$l_{1,2}$	=	ratio between face endpoints, m
$N_{\text{rays per cell}}$	=	number of rays emitted from one cell
$N_{\text{total rays}}$	=	initial number of rays for an entire computational domain
n_a	=	atom number density, m^{-3}
n_e	=	electron number density, m^{-3}
n^+	=	ion number density, m^{-3}
Q_{emis}	=	total integrated emission coefficient, $\text{W/cm}^3\text{-sr}$
$Q_{\text{emis},k}$	=	accumulated atomic emission lines from $i = 1$ to k, $\text{W/cm}^3\text{-sr}$
$Q_{\text{emis},\lambda}$	=	partially integrated emission coefficient, $\text{W/cm}^3\text{-sr}$
q_R	=	radiative heat flux, W/m^2
q_c	=	convective heat flux, W/m^2
R	=	random number, dimensionless
R_c	=	radius of curvature, m
r	=	radial component of photon travel distance in a cell, m
S	=	distance from stagnation point, m
S_d	=	distance from emission point to cell-face intersection point, m
s_x, s_y, s_z	=	directional cosines in a Cartesian coordinate system
T_{rot}	=	rotational temperature, K
T_{trn}	=	translational temperature, K
T_{vib}	=	vibrational temperature, K
T_e	=	electron temperature, K
V_{cell}	=	cell volume, m^3
V_∞	=	freestream velocity, m/s
X	=	horizontal coordinate of direct simulation Monte Carlo domain for the Stardust geometry, m
x_i, y_i, z_i	=	intersection points of a photon bundle with a cell face, m
x_e, y_e	=	emission locations, m
x_1, x_2	=	coordinates of cell boundary along X axis, m
Y	=	vertical coordinate of direct simulation Monte Carlo domain for the Stardust geometry, m
y_1, y_2	=	coordinates of cell boundary along Y axis, m
Z	=	horizontal coordinate of photon Monte Carlo domain for the Stardust geometry, m
α	=	optical length, dimensionless
ε_i	=	emission coefficient of a bound-bound transition at the line-center wavelength, $\text{W/cm}^3\text{-sr}$
ε_λ	=	emission coefficient at a wavelength, $\text{W/cm}^3\text{-}\mu\text{m-sr}$
θ	=	polar angle, rad
κ_λ	=	absorption coefficient, cm^{-1}
λ	=	wavelength, Å
λ_{k_1}	=	wavelength at line-center index k_1, Å
λ_{k_2}	=	wavelength at line-center index k_2, Å
ρ_∞	=	freestream mass density, kg/m^3

Presented as Paper 2010 at the 48th AIAA Aerospace Sciences Meeting including the New Horizons Forum and Aerospace Exposition, Orlando, Florida, 4–7 January 2010; received 28 September 2010; revision received 6 April 2011; accepted for publication 9 April 2011. Copyright © 2011 by the American Institute of Aeronautics and Astronautics, Inc. All rights reserved. Copies of this paper may be made for personal or internal use, on condition that the copier pay the $10.00 per-copy fee to the Copyright Clearance Center, Inc., 222 Rosewood Drive, Danvers, MA 01923; include the code 0887-8722/12 and $10.00 in correspondence with the CCC.

*Graduate Student, Department of Aerospace Engineering; currently Postdoctoral Fellow, Department of Aerospace Engineering. Member AIAA.

†Postdoctoral Fellow, Department of Aerospace Engineering. Member AIAA.

‡Professor, Department of Aerospace Engineering. Associate Fellow AIAA.

§Shaffer and George Professor of Engineering. Associate Fellow AIAA.

$\phi(\lambda)$ = line broadening function, μm^{-1}
φ = cell-face intersection angle, rad
ψ = azimuthal angle, rad

Subscripts

cell = computational cell volume
cross section = cell cross section
emis = emission
i, j = index of cell
k = line center index
max = maximum value
min = minimum value
total = all cells of computational domain
θ = polar angle
λ = wavelength
ψ = azimuthal angle
∞ = freestream

Superscripts

$*$ = normalized quantity

I. Introduction

DURING high-speed reentry into Earth's atmosphere, spacecraft such as the Stardust [1,2] or Crew Exploration Vehicle [3] experience hypersonic nonequilibrium flow conditions that dissociate molecules and ionize atoms. These complex phenomena occurring behind the shock wave lead to high temperature flows and ionization that generate a severe heating load on the thermal protection system (TPS) and cause radar communications blackout to the vehicle. Since the internal energy states of atomic species are strongly excited for high-Mach-number conditions, the radiative contribution to the total heat load is significant.

If the radiative heat load is sufficiently strong, the internal energy distribution of the flow species can be altered, which requires the development of spectrally accurate radiation heat transfer modeling coupled to the flow. In addition, radiative heat energy within the shock layer may influence the ablative species concentration released from the vehicle surface. For these reasons, radiative heat transfer must be considered in the design process of a vehicle, and radiation analyses coupled with flow solvers have to be implemented to improve the reliability during the vehicle design stage.

Flowfield and radiation modeling have been performed in the analysis of Stardust [1,2,4–7] and Fire II [8] vehicles, using established radiation models such as the Langley Optimized Radiative Nonequilibrium (LORAN) code [9] and the Nonequilibrium Air Radiation (NEQAIR) code [10]. In addition, coupled flowfield-radiation interactions have also been performed for the Huygens probe for conditions close to peak heating for reentry into the atmosphere of Titan, Saturn's largest moon [11]. In that study, the viscous shock layer (VSL) technique for the stagnation streamline of flowfield calculation and a modified smeared-rotational band model for the radiation calculation were combined to reduce CPU time rather than solving the full Navier–Stokes equations and a line-by-line radiation model, such as LORAN and NEQAIR.

Recently, closely coupled radiation calculations with advanced hypersonic continuum fluid dynamics (CFD) tools, such as DPLR [12] and LAURA [13], and a newly developed efficient line-by-line radiation database based on NEQAIR [14] have been performed for the Stardust and Fire II reentry conditions [15,16]. A one-dimensional tangent slab (TS) method to solve the radiative transport equation (RTE), using the exact analytical solutions based on exponential integrals [17], was used. The coupled CFD-radiation studies assumed the governing electronic temperature to be equal to the heavy particle translational temperature (in the case of DPLR) or the vibrational temperature (LAURA).

However, under transitional flow conditions, continuum breakdown occurs [18]. Therefore, kinetic methods, such as direct simulation Monte Carlo (DSMC) [19], are required to simulate high-Mach-number reentry flowfields. Modeling of chemical reactions including ionization and energy exchange processes has been successfully implemented in DSMC for the Stardust blunt body between 68.9 and 100-km altitudes [20], but radiation coupling was not considered. Since the electronic excited state populations of atoms are produced predominantly due to collisions with electrons, an accurate model of the molecular nitrogen collisions with electrons was included in the DSMC simulations of Ozawa, Zhong, and Levin [20]. This model is also used in the work presented here because the precise modeling of electron temperature is needed to accurately simulate the vacuum-ultraviolet shock-layer radiation. In other DSMC simulations, Gallis and Harvey [21,22] modeled nonequilibrium thermal radiation as well as electronic excitation processes to investigate the radiation effect on the flowfield. However, for their method, accurate cross sections for electronic excitation and absorption coefficients were required, and the uncertainty in these cross sections could not be assessed for all of the required species and electronic states. Recently, state-specific electronic state excitations for a few key energy levels have been modeled in DSMC and, in future work, may be coupled with radiative transport [23].

In the simulation of coupled hypersonic shock-layer radiation, the fidelity of both the gas dynamic approach as well as the RTE must be considered. The statistical radiative transport using the photon Monte Carlo (PMC) approach has been successfully used to simulate radiation for arbitrarily complex geometries and flow conditions [24–26]. The approach is basically three-dimensional and is important for modeling radiative transport in optically thick media, where the optical thickness gradients may be quite high. The PMC approach may be applied to both continuum and particle-based gas dynamics methods. When closely coupled with a flowfield solver, the advantage of a fully three-dimensional method over the one-dimensional tangent slab approach is to account for the fact that the radiation transport is nonlocal. The disadvantage of this model is that the computational cost for coupling with the flow solver is more expensive than a TS approximation. Therefore, in preliminary analyses and for design processes of simple geometries, TS may be preferred over PMC.

In Ozawa et al. [27], DSMC simulations were loosely coupled with the particle-based photon Monte Carlo (p-PMC) method for Stardust reentry flow conditions. To efficiently solve the radiative transport equation for the highly nonequilibrium gas, emission and absorption coefficient databases [14,28] based on the NEQAIR model were generated. For Earth reentry under those conditions, atomic nitrogen and oxygen radiation effects are the major contributions to the total radiation [6,7,27]. In that work, the influence of the radiative energy on the flowfield characteristics was considered. However, the computational load for the loosely coupled DSMC—p-PMC calculations was very high and is not easily extended to modeling the freestream conditions along a reentry trajectory. Coupled CFD-radiation simulations are also computationally intensive. To improve the PMC radiative transport efficiency, a two-dimensional, axisymmetric finite-volume-based photon Monte Carlo (FV-PMC) method was developed for a body-fitted grid and coupled with a CFD solver to simulate flowfield-radiation interaction during reentry [29]. In the FV-PMC method, the emissive energy associated with an energy bundle is based on the cell properties rather than on computational particles. Because both the emissive energy and the absorption coefficient are based on the macroparameters of particle number density and temperature, the use of cell-based quantities is not a limitation of the method. Similarly, the absorption of a photon bundle is calculated based on the average cell absorption coefficient rather than on the intersection of photon bundles with computational particles.

The objective of this work is to simulate transitional hypersonic flow using DSMC coupled with a finite-volume PMC-radiation approach optimized for a DSMC Cartesian-based grid. With the ability to perform coupled simulations, the effect of radiation on the flow structure for different degrees of hypersonic nonequilibrium can be understood. In addition, the change in convective and radiative heat fluxes along a reentry trajectory that extends from the rarefied

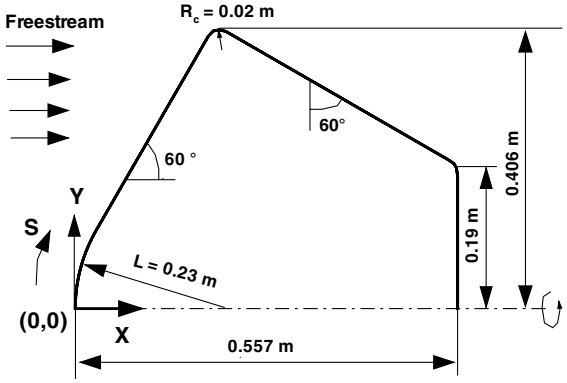

Fig. 1 Stardust geometric configuration.

through the continuum flow regime using DSMC will be characterized. Specifically, in this work, the Stardust blunt body, the fastest human-made object to reenter the atmosphere, is chosen, and four altitudes along the reentry trajectory are considered: 81 km (transitional flow regime), 71.9 km, 65.4 km (near-continuum), and 61.8 km (peak-heating). Since these results are the first DSMC-coupled FV-PMC simulations to be performed along a reentry trajectory, comparisons will be presented with earlier CFD results as well as semiempirical correlations. The former results have been computed assuming that the surface is fully catalytic with respect to atomic species recombination. Therefore, to compare the present DSMC simulations of the convective heat flux to these earlier results, the extension of the present DSMC gas-surface interaction model to include fully catalytic conditions is discussed.

II. DSMC Flow Modeling

We review here the physical models and the numerical parameters used in the DSMC simulations and discuss the manner of coupling between the radiation energy and the flowfield calculations. We then present flowfield results at two freestream conditions that illustrate the range of nonequilibrium conditions in the Stardust flow trajectory.

A. Physical Models and Numerical Parameters

To model hypersonic reentry flow, a number of physical models related to the ionized, chemically reacting flow as well as the thermochemical nonequilibrium must be considered. That flow was simulated using the Statistical Modeling in Low-Density Environment (SMILE) [30] DSMC computational tool. The majorant frequency scheme was employed for modeling the molecular collision frequency [31], and the variable hard sphere (VHS) model was used for modeling the interaction between particles [32]. The Borgnakke–Larsen [33] model with temperature-dependent rotational and vibrational relaxation numbers was used for modeling rotation-translation (R-T) and vibration-translation (V-T) energy transfer between neutral species. The Millikan and White (MW) [34] and Parker's rates [35] were used to model V-T and R-T relaxation rates, respectively. At high temperatures, both vibrational and rotational collision numbers should converge to a similar constant number due to the strong vibration-rotation coupling. The MW vibrational collision number, however, implies an unrealistically large cross section for vibrational relaxation at high temperature. Therefore, the vibrational excitation cross section for nitrogen was adjusted to ensure that the V-T collision numbers were consistent with the rotational collision number [36]. Chemical reactions involving both neutral and charged species were modeled using the total collision energy (TCE) model [19], with a total of 11 species (N, O, N^+, O^+, N_2, O_2, NO, N_2^+, O_2^+, NO^+, and e^-) modeled in 51 chemical reactions, including five ionization processes [37,38]. The thermochemical model presented here is limited to a nonablating flow. The inclusion of ablation species would require a much more extensive model that is beyond the scope of the present work but may be considered later.

The electron concentration in the flow was sufficiently low such that the computational time step was associated with molecular collisions rather than with the electron collision frequency. In our simulations, the electron movement depended on the average ion velocity per cell, and the charge neutrality assumption was used [20]. The electron velocity, or energy, was concurrently stored per simulated electron and was used to calculate the collision frequency, energy exchange, and chemical reaction rates between electrons and heavy particles. Electron-vibrational relaxation was modeled using Lee's relaxation model for electron collisions with N_2 [39]. Finally, the gas-surface interaction was modeled using the Maxwell model with total energy and momentum accommodation. The surface wall temperature was assumed to be 3000 K along the vehicle surface for all altitudes [6], and full charge recombination at the vehicle surface, a standard assumption in weakly ionized flows, was assumed [40].

DSMC simulations were performed for the Stardust blunt body geometry shown in Fig. 1 with the freestream conditions given in Table 1. The selection of time step, cell size, computational domain, and total number of simulated molecules was investigated to obtain results independent of these DSMC numerical parameters. Table 1 summarizes the number of simulated particles as well as collisional and macroparameter sampling cells used for the four altitude cases. The total number of time steps was about 100,000, with a time step of 2.0×10^{-8} s used for the 81 to 65.4-km cases and 1.0×10^{-8} s used for the 61.8-km case. Macroparameter sampling was started after 30,000 time steps, which was a sufficient time for the flowfield and heat flux to reach steady state. In summary, heat flux values along the surface and flow macroparameters were found to be converged for these numerical parameters.

As will be shown in Sec. II.B, the flow consists mainly of atomic N and O within the shock layer of the Stardust vehicle. The collision rate between free electrons and atomic and molecular species in a cell is sufficiently high such that it can be assumed that the energy exchange between free electrons and the internal energies of heavy species is fast and completed in a single time step. Therefore, the radiative heat source term $\nabla \cdot q_R$, calculated by the FV-PMC method, is redistributed among the translational and internal energy modes of gas species in proportion to the degrees of freedom of the translational, rotational, and vibrational modes of the species [27]. The DSMC simulation employs a collisional-level and a macroparameter-level Cartesian grid structure. Radiative energy exchange

Table 1 Freestream and DSMC numerical parameters

Parameter	61.8 km	65.4 km	71.9 km	81.0 km
Freestream:				
Temperature, K	235.0	224	221.42	217.6
Number density, m^{-3}	4.383×10^{21}	1.603×10^{21}	8.65×10^{20}	2.64×10^{20}
Speed, km/s	11.4	12.0	12.4	12.6
O_2 mole fraction, %	20.6	22.1	23.7	23.7
N_2 mole fraction, %	79.4	77.9	76.3	76.2
Numerical:				
$K_{n,\infty}$ ($L = 0.23$ m)	6.3×10^{-4}	1.2×10^{-3}	3.2×10^{-3}	1.0×10^{-2}
Number of simulated particles	34.4 million	11.7 million	6.7 million	2.7 million
Number of collisional cells	3.5 million	1.1 million	0.68 million	0.26 million

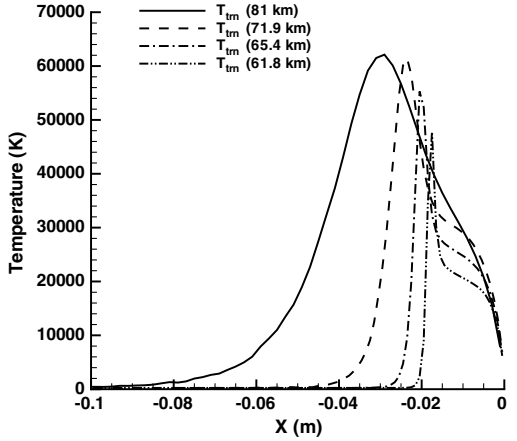

Fig. 2 Variation of translational temperature along the stagnation streamline from transitional to peak-heating regime.

was simulated at the collisional cell level; however, the radiative source term was obtained using the macroparameter cells.

B. DSMC Flow Modeling Results Without Radiation Coupling

The DSMC calculations were performed for the four freestream conditions given in Table 1. Figure 2 shows the profile of translational temperatures along the stagnation streamline at each altitude. It is clearly seen that the shock standoff distance increases as the altitude becomes higher because the flow rarefaction increases. A temperature overshoot is observed for altitudes below 71.9 km as the temperature profiles take on more continuumlike behavior. As we discuss later, the maximum internal temperatures are nearly 20,000 K for the lowest altitude considered. Thus, as altitude is lowered, the degree of thermal nonequilibrium decreases and the flow becomes more continuumlike. To understand the change in flow features at a more detailed level, two altitude cases, 71.9 and 61.8 km, were examined. The 71.9-km case is chosen instead of the highest altitude, 81 km, because there are a sufficient number of collisions that result in thermal excitation and ionization reactions in the stagnation region. Also, as will be discussed in Sec. V, the radiation coupling at 81 km will be shown to be negligible.

For 71.9 km, Figs. 3 and 4 show the stagnation streamline profiles of the flow temperatures and chemical species number densities as well as contour fields in the forebody region for the electron number densities and temperatures, respectively. The degree of thermal nonequilibrium is strong with the maximum translational temperature as high as 60,000 K compared to the internal and electron temperatures being lower than 24,000 K. At this altitude, the differences among rotational, vibrational, and electron temperatures are small. The simulations predict the temperature overshoot to be between $X = -0.03$ and -0.02 m, but the difference between the temperatures decreases to less than 10,000 K from $X = -0.02$ m to the surface. Because of the high dissociation rates, atomic neutrals followed by their ionic species are dominant in the shock layer, and ionization occurs within $X = -0.02$ m at this altitude. The maximum degree of ionization was found to be approximately 7%, and the maximum electron temperature is about 22,000 K at this altitude.

The second set of DSMC calculations carried out at 61.8-km altitude correspond to peak heating for the Stardust reentry trajectory. These computations are costly for DSMC but were undertaken because the maximum radiation and heat flux to the surface occurs at

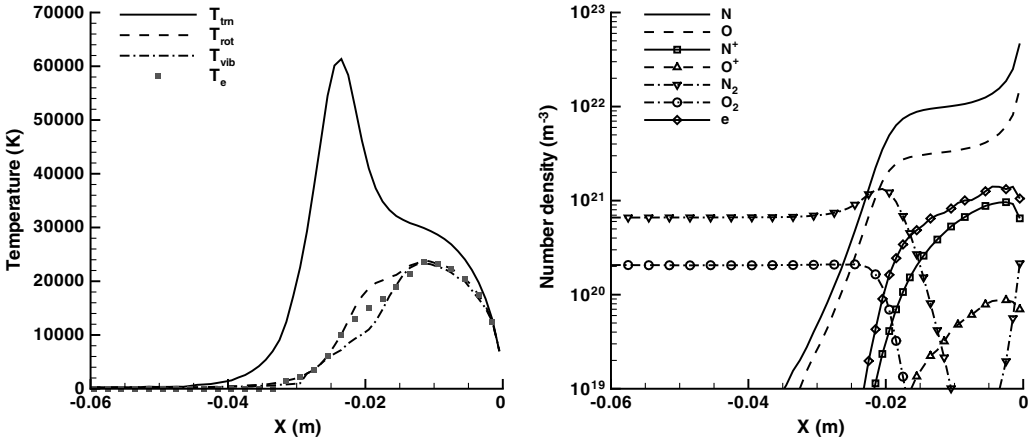

Fig. 3 Distributions of temperatures (left) and number densities (right) along the stagnation streamline at the 71.9-km altitude.

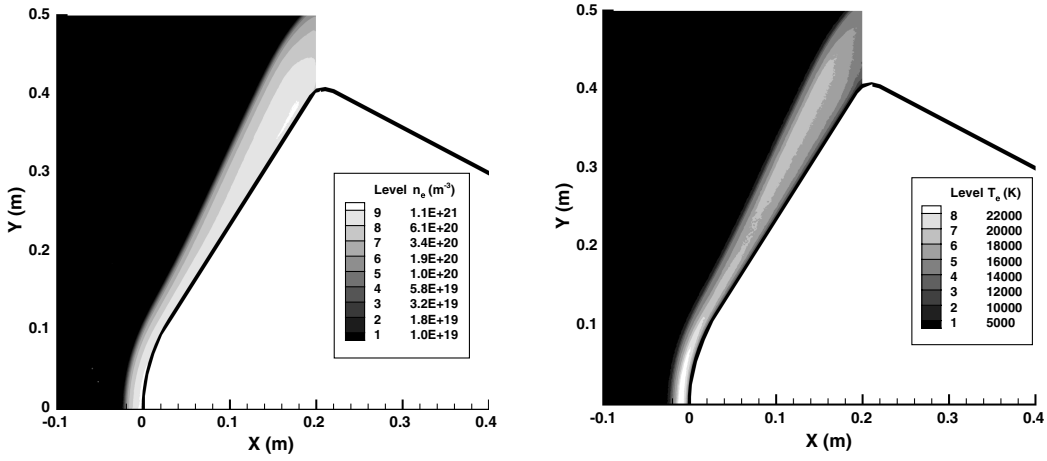

Fig. 4 Contours of the electron number density (left) and electron temperature (right) at the 71.9-km altitude.

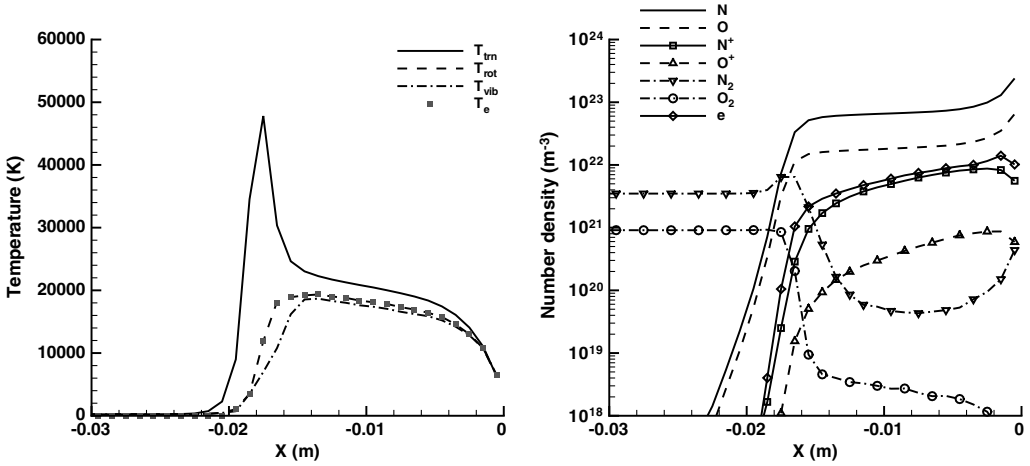

Fig. 5 Distributions of temperatures (left) and number densities (right) along the stagnation streamline at the 61.8-km altitude.

this altitude. The flowfield at 61.8 km without radiation coupling along the stagnation streamline is shown in Fig. 5. The differences between the translational temperature and the other internal temperatures decrease at this altitude compared to those for higher altitudes because the higher collision rate at this lower altitude brings the flow closer to thermal equilibrium. Similarly, the differences among rotational, vibrational, and electron temperatures are negligibly small, and the maximum electron temperature is approximately 19,000 K. At this altitude, the overshoot phenomenon can be seen between $X = -0.02$ and -0.015 m, and the differences between translational and the other temperatures are less than 4,000 K between $X = -0.015$ m and the surface. Figure 6 shows contour plots of the electron number density and electron temperature. The regions of high electron number density and electron temperature are seen to be compressed as compared to those for the 71.9-km altitude shown in Fig. 4, which produces high gradients of electron concentration and temperature. Because of the high dissociation rates, molecules are mostly dissociated inside the shock and the maximum degree of ionization is approximately 8%.

III. Modeling of a Fully Catalytic Wall Condition in DSMC

In our previous DSMC flow modeling of the Stardust vehicle, charge recombination was assumed at the vehicle surface with no additional energy transfer to the flowfield or surface [20,27]. This condition is also typically assumed in CFD simulations; however, for neutral atomic species collisions with the wall, a surface catalycity model is usually specified. In particular, the spacecraft wall, depending on its material, can act as a catalyst to cause atomic oxygen and nitrogen recombination at the wall [6]:

$$O + O \rightarrow O_2 + 5.08 \text{ eV} \tag{1}$$

$$N + N \rightarrow N_2 + 9.8 \text{ eV} \tag{2}$$

In a strong hypersonic shock layer, there is a significant amount of molecular dissociation so that the type of gas-wall surface model assumed will strongly affect the concentrations of atomic O or N, or their respective molecular diatomic species, in the boundary layer. In addition, the previous recombination reactions are highly exothermic so that the convective heat flux to the wall can be significantly affected by the catalytic model as well. Since the DSMC simulations presented here were applied to freestream conditions close to peak heating, they will be compared with CFD simulations. In particular, the CFD simulations of Olynick et al. [1] were obtained using the common assumption of fully catalytic recombination. To enable a closer comparison between the two different gas dynamic approaches, the DSMC surface modeling was extended to include a fully catalytic recombination. The assumption of a fully catalytic wall was implemented in the DSMC in the following manner. When DSMC particles representing atomic oxygen or nitrogen atoms impact the surface, a second atomic oxygen or nitrogen atom particle is removed from that cell, the corresponding molecular species is created and introduced into the flow, and the heat of recombination is distributed among all particles within that cell and within that time step. The released energy from the atomic recombination is redistributed among the translational, rotational, and vibrational modes of all of the molecules (including those just formed during the time step). The distributions of energy among the different modes were performed assuming equipartition. In subsequent time steps,

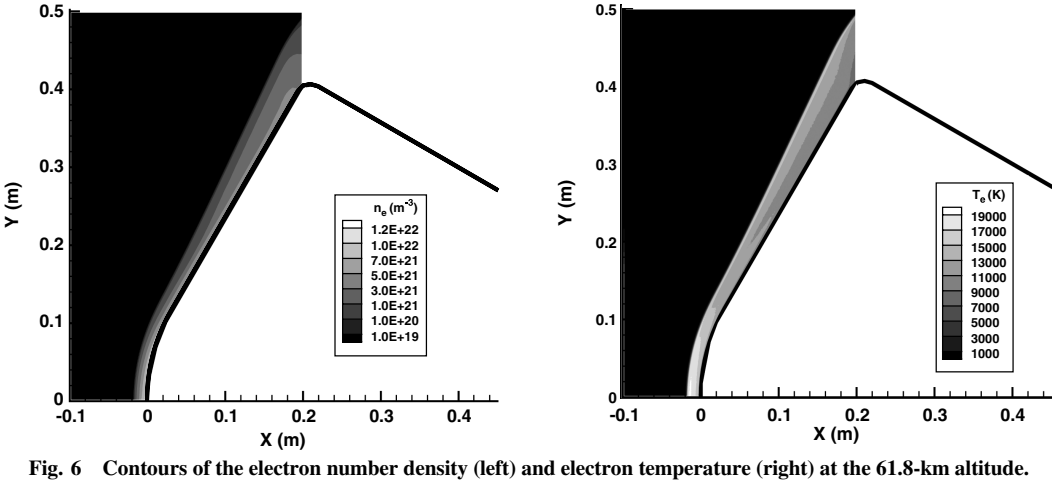

Fig. 6 Contours of the electron number density (left) and electron temperature (right) at the 61.8-km altitude.

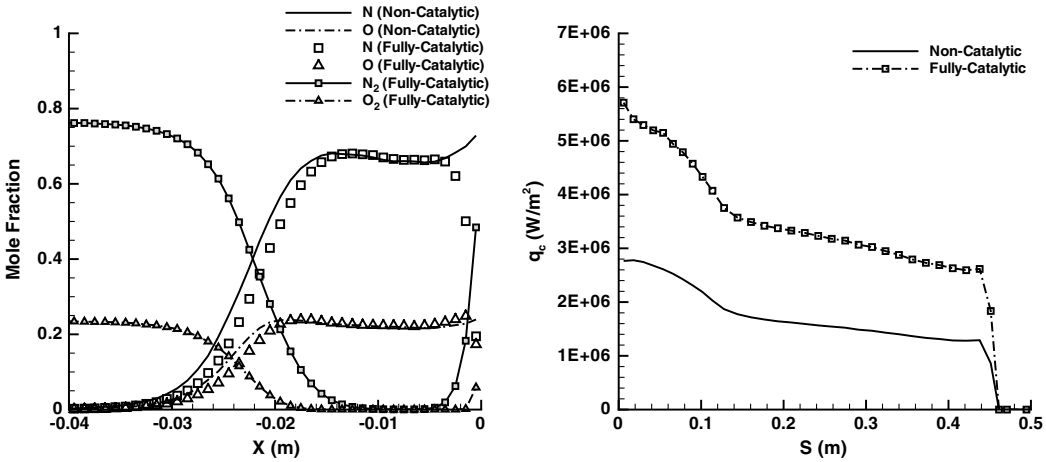

Fig. 7 Comparison of mole fraction of atomic N and O species along the stagnation streamline (left) and convective heat flux along the Stardust forebody surface (right) due to surface catalytic recombination at the 71.9-km altitude.

this increased internal molecular energy due to recombination can be transferred to other species in the flow through collisions and increases the convective heat flux by gas-surface collisions.

Figure 7 shows the sensitivity of the predicted mole fractions and heat flux profiles for atomic O and N to a noncatalytic wall condition (baseline) versus the new fully catalytic surface condition at 71.9-km altitude. It can be seen that, due to the surface catalytic recombination processes given in Eqs. (1) and (2), the mole fractions of N_2 and O_2 increase, whereas those of N and O for the fully catalytic case decrease near the surface compared to those of N and O for the noncatalytic case. Figure 7 also shows a comparison of the convective heat flux along the forebody surface with and without surface catalytic recombination. Since heat is released during the surface recombination processes, the DSMC predicted convective heat flux correctly increases for a fully catalytic surface compared to that for a noncatalytic condition.

IV. Finite-Volume Photon Monte Carlo Radiation

A. The Photon Monte Carlo Tracing Approach

A two-dimensional axisymmetric finite-volume based PMC (FV-PMC) code was developed using the same macroparameter grid structure of the DSMC code and the same physical model and principles as in the PMC three-dimensional model [29]. The FV-PMC method simulates radiation by tracing photon bundles from an emission point to a termination location. The locations and directions of the emitting photon bundles in each cell are determined using random number relations. The direction of each ray is selected randomly by

$$\psi = 2\pi R_\psi \tag{3}$$

$$\theta = \cos^{-1}(1 - 2R_\theta) \tag{4}$$

where R_ψ and R_θ are uniformly distributed random numbers from 0 to 1.

The FV-PMC tracing scheme uses the energy partitioning method [29], which traces a photon bundle and calculates the fraction of energy absorbed by each cell that the bundle passes through. To accomplish this, the distance S_d that the bundle travels as it passes through the cell and to the particular cell face with which it intersects has to be determined. That distance is used to calculate the quantity of energy absorbed, and the intersection coordinates on the cell face of the photon bundle become the new initial location of the ray tracing in the next cell. The following equations give the cell face intersection coordinates in terms of the emission location coordinates and directional vectors of a photon ray. The intersection point is written as

$$x_i = x_e + S_d s_x \tag{5}$$

$$y_i = y_e + S_d s_y \tag{6}$$

$$z_i = S_d s_z \tag{7}$$

where x_i, y_i, and z_i are the intersection coordinates with the cell face in the x, y, and z directions, respectively; S_d is the distance traveled through the cell; x_e and y_e are the emission locations in the cell; and s_x, s_y, and s_z are the directional cosines. Figure 8 shows a schematic diagram of the method used to determine the intersected cell face in a single cell. The four face conditions for ray tracing in a two-dimensional axisymmetric PMC on the DSMC macroparameter grid are defined as follows:

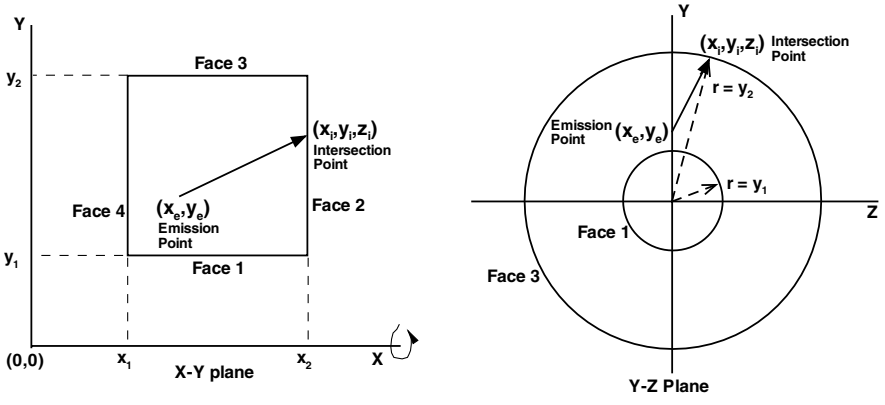

Fig. 8 Schematic diagram of ray tracing in one cell on *X-Y* (left) and *Y-Z* plane (right).

$$\text{face 1: } x_1 < x < x_2, \qquad r = y_1 \tag{8}$$

$$\text{face 2: } x = x_2, \qquad y_1 < r < y_2 \tag{9}$$

$$\text{face 3: } x_1 < x < x_2, \qquad r = y_2 \tag{10}$$

$$\text{face 4: } x = x_1, \qquad y_1 < r < y_2 \tag{11}$$

The procedure to determine which face will be intersected by the photon bundle begins with testing whether face 1 or 3 satisfies the criteria for a valid intersection. The distance traveled by a photon bundle through the cell (S_d) and the radial distance r are calculated by assuming that the photon bundle will intersect either face 1 or 3, or

$$l_{1,2} = -B \pm \sqrt{B^2 - C} \tag{12}$$

where

$$B = (s_y y_e)/(1 - s_x^2) \tag{13}$$

$$C = (y_e^2 - y_{2\text{ or }1}^2)/(1 - s_x^2) \tag{14}$$

There are two solutions to Eq. (12) for l, but the valid intersection must be $l_{1\text{ or }2} > 0$ and $x_1 < x_i < x_2$. If l_1 or l_2 satisfies these conditions, then S_d is set to that l value. If face 1 or 3 is found not to be a valid intersection face, then faces 2 and 4 are examined by calculating the quantities

$$S_d = \frac{x_2(\text{or } x_1) - x_e}{s_x} \tag{15}$$

$$r = \sqrt{(S_d s_y + y_e)^2 + (S_d s_z)^2} \tag{16}$$

Likewise, if the two conditions that $S_d > 0$ and $y_1 < r < y_2$ are satisfied, then either face 2 or 4 is a valid intersected face, and the intersection point (x_i, y_i) becomes the new emission location (x_e, y_e) of the next cell.

After determining the intersection point and the corresponding distance traveled, the intersection point must be transformed back into the original X-Y plane to keep the computation two-dimensional. Also, the direction of the photon bundle must be adjusted to reflect this rotation back into the original plane (RHS of Fig. 8). This new azimuthal angle of the photon bundle is calculated using $\psi - \varphi$ (azimuthal angle, face intersection angle), where

$$\psi = \tan^{-1}\left(\frac{s_z}{s_y}\right) \tag{17}$$

$$\varphi = \tan^{-1}\left(\frac{z_i}{y_i}\right) \tag{18}$$

As the photon travels through the computational domain, the energy associated with the photon bundle is decreased due to the absorptivity of the traversed cell. The optical length traveled through the cell can be calculated as

$$\alpha = 1 - e^{-\kappa_\lambda S_d} \tag{19}$$

where κ_λ denotes the cell absorption coefficient. The amount of energy absorbed by the cell E_{abs} and the energy carried by the photon bundle E_{trans} can be calculated as

$$E_{\text{abs}} = \alpha E_{\text{bundle}} \tag{20}$$

$$E_{\text{trans}} = E_{\text{bundle}} - E_{\text{abs}} \tag{21}$$

The next cell the ray will enter is also determined by Eqs. (5–16). The absorbed energy E_{abs} is calculated by tracing a large number of bundles using the random number relations [Eqs. (3) and (4)] and Eqs. (5–16). Therefore, as the number of photon bundles increases, the standard deviation in each cell is reduced. For a nongray medium, a ray is randomly assigned a wavelength using an emission random number database (ERND) for the cell species, as is discussed in Sec. IV.B.

Finally, the divergence of the radiative heat flux ($\nabla \cdot q_R$) is calculated as the difference between the emission and absorption energy for each cell by

$$(\nabla \cdot q_R)_{i,j} = \left(\frac{E_{\text{emis}} - E_{\text{abs}}}{V_{\text{cell}}}\right)_{i,j} \tag{22}$$

where i and j are cell indices, and V_{cell} denotes a cell volume.

Generally, the number of rays emitted from an individual cell is determined according to the fraction of emissive cell energy to total emissive energy as follows:

$$N_{\text{rays per cell}} = N_{\text{total rays}} \times \frac{E_{\text{cell}}}{E_{\text{total}}} \tag{23}$$

where $N_{\text{rays per cell}}$ and E_{cell} are the number of rays emitted from a cell and the corresponding total emission energy of the cell, respectively; $N_{\text{total rays}}$ is an initial number of rays specified by the user; and E_{total} is the total emission energy in the entire domain, which can be obtained by summing the emission energy of each cell (E_{cell}). Since the emission energy of each cell (E_{cell}) is proportional to the cell volume, the number of rays emitted from cells located along the symmetry axis is very small. Hence, the statistical deviation in the net radiative heat flux near the symmetry axis is higher than that in the outer cells, but the former is usually the main region of interest. To avoid a large statistical variation near the symmetry axis, the number of rays per cell is redefined based on the cell area instead of the cell volume [29] and is expressed as

$$N_{\text{rays per cell}} = N_{\text{total rays}} \times \frac{E_{\text{cell cross section}}}{E_{\text{total cross section}}} \tag{24}$$

where $E_{\text{cell cross section}}$ is the emission per volume times the cell area, and $E_{\text{total cross section}}$ is a summation of $E_{\text{cell cross section}}$ values over the entire domain. Use of this relationship helps us to obtain roughly an equal number of photon rays per cell, which in turn causes the high emission rate per volume near the symmetry axis to generate a large number of photon bundles and improve the symmetry axis statistics. Even though the number of photon rays is specified based on the cell area, the emission energy per ray is determined by dividing the cell emissive power by the number of photon rays. Hence, compared to the volume weighted scheme, cells near the symmetry axis will emit a larger number of weaker photon rays, whereas cells further away from the symmetry axis will emit fewer photon rays. Therefore, for those cells off of the symmetry axis, each photon ray will be stronger than the corresponding ones emitted in the volume-weighted scheme.

For a nongray medium, an emitted ray is assigned by a random wavelength to be associated with an energy bundle. This wavelength is determined from a spectral module using a random number database for the related species in the cell, as will be discussed in the next subsection.

B. Wavelength Selection in the PMC Procedure

The emitting species for a given ray is selected, based on the ratio of the emitting energies for each species to the total emission. For a given photon bundle, a wavelength is selected by comparing a random number R_λ to the ratio of the partially integrated emission to the total integrated emission:

$$R_\lambda = \frac{Q_{\text{emis},\lambda}}{Q_{\text{emis}}} = \frac{\int_{\lambda_{\min}}^{\lambda} \varepsilon_\lambda \, d\lambda}{\int_{\lambda_{\min}}^{\lambda_{\max}} \varepsilon_\lambda \, d\lambda} \tag{25}$$

where λ is the corresponding wavelength of a photon bundle, and R_λ is a random number uniformly distributed from 0 to 1. A bisection method is used to select the value of wavelength between $\lambda_{\min}$ and $\lambda_{\max}$ as is needed to evaluate Eq. (25). An emission random number databases (ERND) was developed for conditions that occur in nonequilibrium flows [28], based on our NEQAIR-based emission and absorption coefficient database [14].

In the aforementioned atomic database, the electronic excited population is calculated using the quasi-steady-state (QSS) model as a function of electron temperature T_e, electron number density n_e, and the ratio of ion to neutral number density (n^+/n_a). Emission and absorption coefficients are calculated as a function of T_e, n_e, n^+/n_a, and translational temperature T_{trn}. For N and O, 170 and 86 atomic lines are included in the databases, respectively, and the atomic lines are sorted in order of increasing wavelength. Based on investigations of hypersonic reentry flowfields [15,20], the important range of the electron temperature T_e has been identified as 1,000–28,000 K, and similarly for electron number densities n_e as 1×10^{13}–4×10^{16} cm^{-3}. For each atomic line, normalized accumulated emission coefficients have been databased for equidistant values of $T_e^{0.1}$ (70 points) and $[\log(n_e)]^{0.1}$ (50 points). For bound-free transitions, partially integrated emission is stored as a function of λ for each T_e, n_e, and n^+/n_a condition. For continuum transitions, the considered wavelength range is from 500 to 6000 Å with a resolution of 10 Å.

Once the emission and absorption coefficient databases are available, separate ERND bound-bound, bound-free, and free-free continuum transition databases are constructed. Note that, however, for the Stardust reentry cases considered here, the contribution of free-free transitions is negligible and is not considered further. For bound-bound transitions, the line-center wavelength λ_k (Å) and the normalized accumulated emission coefficient $Q^*_{\text{emis},k}(T_e, n_e, n^+/n_a)$ are stored. The normalized accumulated emission coefficient is calculated as

$$Q^*_{\text{emis},k} = \sum_{i=1}^{k} \varepsilon_i^*(T_e, n_e, n^+/n_a) \tag{26}$$

where $\varepsilon_i^*(T_e, n_e, n^+/n_a)$ is a normalized emission line strength ε_i, which is normalized by n_a. Also, the partially integrated emission is calculated as

$$\begin{aligned} Q^*_{\text{emis},\lambda} &= \int_{\lambda_{\min}}^{\lambda} \varepsilon_\lambda^*(T_e, n_e, n^+/n_a, T_{\text{trn}})\,\mathrm{d}\lambda = \sum_{i \le k_1} \varepsilon_i^*(T_e, n_e, n^+/n_a) \\ &\quad + \sum_{k_1 < i \le k_2} \int_{\lambda - b_{hw,\max}}^{\lambda} \varepsilon_{\lambda,i}^*(T_e, n_e, n^+/n_a, T_{\text{trn}})\,\mathrm{d}\lambda \\ &= Q^*_{\text{emis},k_1}(T_e, n_e, n^+/n_a) + \sum_{k_1 < i \le k_2} \varepsilon_i^* \int_{\lambda - b_{hw,\max}}^{\lambda} \phi(\lambda)\,\mathrm{d}\lambda \end{aligned} \tag{27}$$

where $\phi(\lambda)$ is the line-broadening function. In Eq. (27), the first line index k_1 corresponds to the maximum integer and is selected by determining whether $\lambda_{k1} < \lambda - b_{hw,\max}$, where $b_{hw,\max}$ is the maximum half-width for the type of line-broadening that is assumed. Since we assume that the line-shape is a Voigt profile, we use a constant value of $b_{hw,\max} = 50.0$ Å, a value adequate to cover the half-width for hypersonic flow conditions. The second line index k_2 is the maximum integer selected by $\lambda_{k2} < \lambda + b_{hw,\max}$. The wavelength selection process is the most time-consuming portion of the PMC procedure. To select a wavelength, a bisection method is used following Eq. (25). In the spectral module, k_1 and k_2 are thus efficiently found, and the partially integrated emissions are calculated effectively. Additional details on the wavelength selection procedure and the ERND can be found in Ozawa, Modest, and Levin [28].

C. Validation

To validate the DSMC FV-PMC approach, a series of one-dimensional disks were constructed using the Stardust stagnation streamline flow conditions obtained from the DSMC solution at 71.9 km. Figure 9 (LHS) shows a comparison of the radiative source term ($\nabla \cdot q_R$) obtained from the DSMC–PMC with a tangent slab simulation. In both calculations, atomic N and O radiation including bound-bound and bound-free transitions are considered. For this flow condition, the emitted energy of the photon rays is highly absorbed by the medium because the flow is optically thick. The magnitude of the net radiative heat source is small compared to the emission energy; e.g., at $X = -0.0105$ m, the fraction of the divergence of the radiative heat flux to the emission energy is approximately 1.8%. As is shown in Fig. 9 (LHS), good agreement is achieved between the PMC and TS calculations, and the small differences in the radiative heat source term may be attributed to the small variation in flow properties in the direction normal to the surface. The highest statistical error in the divergence of the heat flux in the stagnation region was found to be less than 5%.

The FV-PMC code is parallelized by assigning columns of cells orthogonal to the surface to each processor. Then each processor traces photons emitted from its column of cells until they are absorbed or leave the domain. Even though a single photon bundle is emitted from a specified cell assigned on a processor, the tracing of this photon bundle is performed on that processor for the entire computational domain. After the tracing is completed by multiple processors in parallel, the main processor gathers the information from the tracing results (absorbed energy) from each processor to compute the radiative source term. Two hundred million photon bundles were traced through the entire domain, taking about 10 CPU hours with 16 processors. Note that, when the volume-based weighting method given in Eq. (23) was used, more than 500 million photon bundles were required to obtain about a 5% statistical error near the symmetry axis. The same level of accuracy was obtained

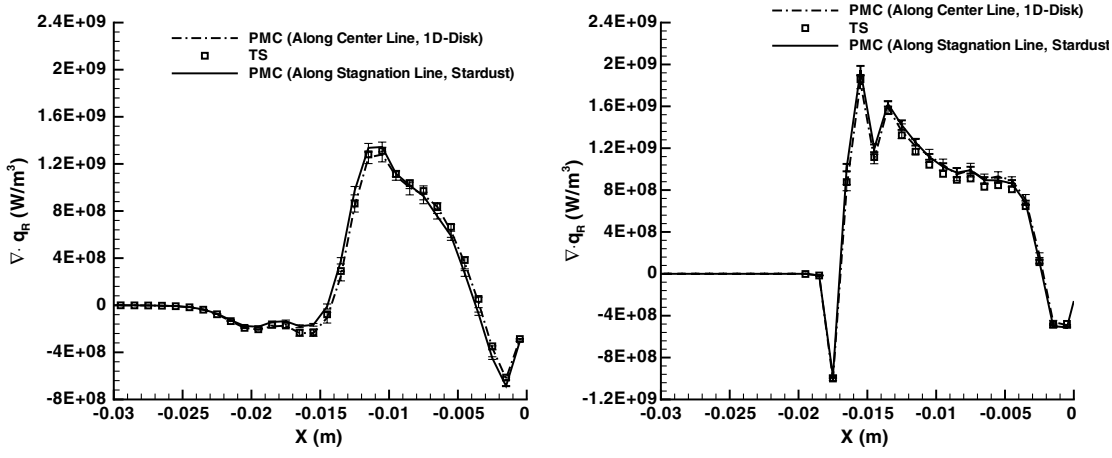

Fig. 9 Comparison of $\nabla \cdot q_R$ along the stagnation streamline among the PMC 1-D disk, PMC Stardust geometry, and 1D-TS at the 71.9-km (LHS) and 61.8-km (RHS) altitudes.

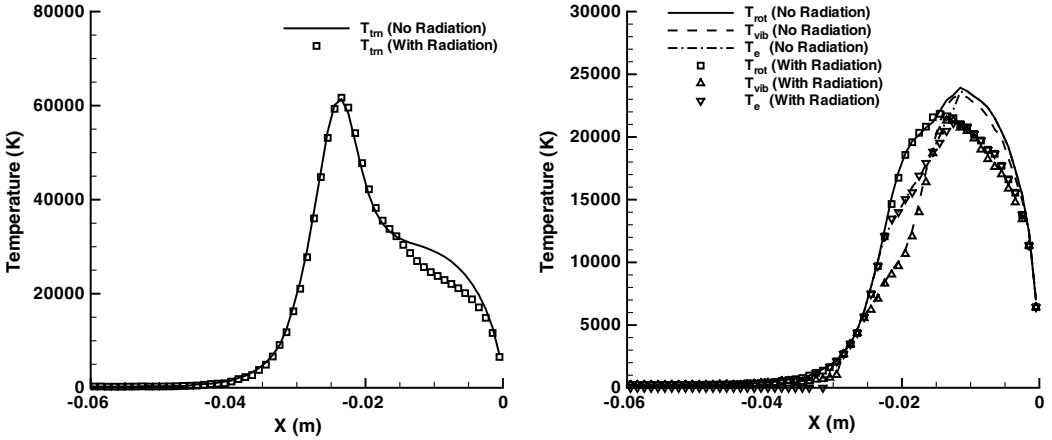

Fig. 10 Comparison of distributions of the translational (left) and rotational, vibrational, and electron (right) temperatures along the stagnation streamline between cases with and without radiation at the 71.9-km altitude.

using the cross-section-based method to determine the number of photon rays per cell given in Eq. (24) at a CPU time savings of more than a factor of 2. The same validation case was performed for the lower altitude of 61.8 km and is shown on the RHS of Fig. 9. Similar to the results from the higher altitude case, the agreement between the radiative heat fluxes predicted by the one-dimensional PMC disk and TS methods is good and is within 5%. Again the emitted energy of the photon rays is highly absorbed by the medium due to the fact that the flow is optically thick. Hence, the magnitude of the net radiative heat source term is as small as 1.2% compared to the total emission energy at $X = -0.0155$ m.

V. Coupled DSMC–PMC Simulation Results

In this section, details of coupled DSMC–PMC simulations for the Stardust reentry vehicle are discussed for the three lowest altitude cases because the flow-radiation coupling was found to be negligible at 81 km. For that case, three iterations of DSMC–PMC-coupled calculation were performed until the convergence of both the flowfield and radiation was achieved. The convective heat flux at the stagnation point (without radiation coupling) was approximately 1.8×10^6 W/m^2, and the radiative heat flux was found to contribute about 16% to the total heat flux. With radiation coupling, the convective heat flux at the stagnation point decreased by only 5%. At 71.9 km, as shown in Figs. 3 and 4, the flow characteristics become transitional in nature, whereas, at the 61.8-km altitude, the flow is continuumlike and corresponds to peak heating for the Stardust reentry trajectory. The change in flowfield and convective heat flux to the vehicle surface due to the radiation will be discussed in detail, for the 71.9 and 61.8-km altitudes, and the results at other altitudes will be summarized. In the coupled DSMC–PMC simulations, the noncatalytic surface boundary condition is assumed, but in Sec. V.D the convective heat fluxes obtained using the extended DSMC catalytic surface boundary condition will be presented and compared with CFD results.

A. Coupled DSMC Calculations with PMC at the 71.9 and 65.4-Kilometer Altitudes

First, we consider the effect of radiation coupling on the shock-layer flowfield. Figure 10 shows a comparison of distributions of the translational, rotational, vibrational, and electron temperatures along the stagnation streamline between two simulations with and without radiation at 71.9 km. The simulation results shown with radiation coupling are those obtained after the final coupling iteration. Along the stagnation streamline, the peak in the radiation profile was found to be located at $X = -0.015$ m (not shown). We have found that the temperature profile remains the same upstream of this location, but, from $X = -0.015$ m to the surface, the effect of radiative cooling on the temperature profile can be observed. After two coupling iterations, the maximum decrease in the translational and internal temperatures was approximately 8000 and 5500 K, respectively, as energy was removed from the flow in the form of radiation. However, in the third iteration, radiative energy was added back to the flow because the amount of energy removed due to the radiation cooling effect was overestimated in the first two iterations. This over-correction causes the gas temperatures to increase after the third coupling iteration. As the coupling is repeated, it is found that the translational and internal temperatures converge. Finally, after the fifth iteration of DSMC–PMC coupling, the translational and internal

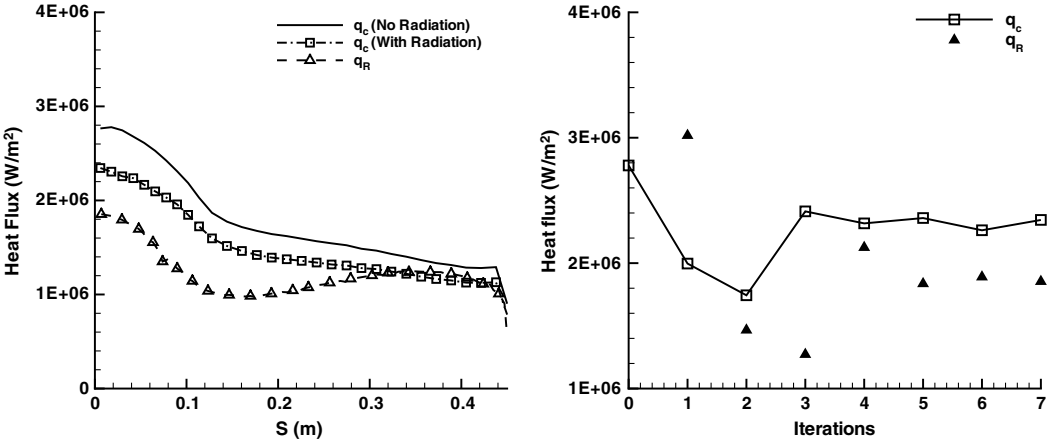

Fig. 11 Comparison of heat flux to the surface for cases with and without radiation along the forebody surface (LHS) and heat flux at the stagnation point for each iteration of DSMC–PMC coupling (RHS) at the 71.9-km altitude. Here, and in subsequent figures, $S = 0$ and 0.436 represent the stagnation point and shoulder of the vehicle, respectively.

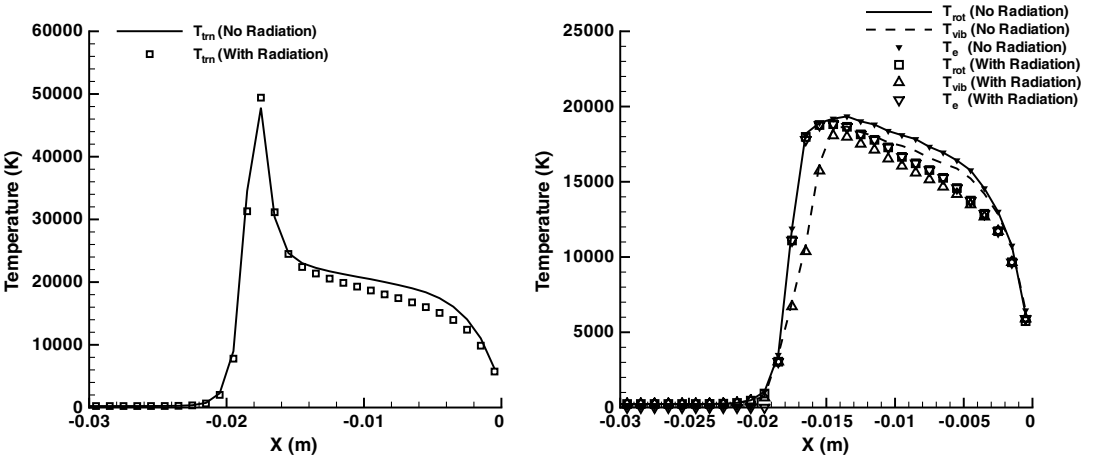

Fig. 12 Comparison of distributions of the translational (left) and rotational, vibrational, and electron (right) temperatures along the stagnation streamline between cases with and without radiation at the 61.8-km altitude.

temperatures were observed to drop by about 5000 and 3500 K, respectively.

Now we turn to the quantities and profiles of heat flux. Figure 11 (LHS) shows a comparison of the convective heat flux and the radiative heat flux without and with the final converged value of radiation to the surface at 71.9 km. Because of the radiation cooling effect, the convective heat flux along the surface from the stagnation point to the shoulder decreases. The maxima in the radiative heat flux are observed to be in both the stagnation region as well as the shoulder because of the high electron number densities and temperatures, as can also be seen in Fig. 4. Figure 11 (RHS) presents the convective and radiative heat flux to the stagnation point as a function of coupling iterations. The results show that, after about four iterations, both convective and radiative heat fluxes are converged within a 5% criteria and that the convective heat flux decreases when coupled to the radiation. The convective heat flux was found to be affected by radiation heat coupling and decreased by 23% after two iterations and 14% after the final coupling iteration. The contribution of radiative heat flux to the total heat flux is about 43% at this altitude. Because the DSMC simulations assumed a noncatalytic surface condition for this case, the convective heating rate is lower than that for the CFD results, which are usually reported for a fully catalytic surface condition [1]. For this reason, the contribution of the radiative flux to the total heat flux is higher than usually shown. However, there are large uncertainties in the degree of the catalytic process, and, in cases where a wall material warrants a noncatalytic model, the results show that the effect of the radiative heating on the total heat flux is not negligible.

At the 65.4-km altitude, the converged DSMC–PMC-coupled results are achieved after the second iteration. The convective heat flux to the surface decreases by 16% due to the radiation, and the translational and internal temperatures drop by 3500 and 2500 K, respectively. The converged radiative heat flux to the stagnation point is 3.07×10^6 W/m^2, which is 47% of the total heat flux, assuming a noncatalytic surface condition in DSMC.

B. Coupled DSMC Calculations with PMC at 61.8 Kilometers

At peak heating, we consider first the effect of radiation on the flowfield and then the importance of radiative coupling on the heat fluxes. Figure 12 shows a comparison of the distributions of the translational, rotational, vibrational, and electron temperatures along the stagnation streamline for cases without and with (final iteration) radiation cooling at the 61.8-km altitude. The DSMC–PMC calculations were iterated until both the flow macroparameters and radiation converged within the 5% criteria, which, at this altitude, occurred after three iterations. Along the stagnation streamline, the radiation peak is located near $X = -0.015$ m, and the effect of radiative cooling on the flow along the stagnation streamline can be seen in the figure between $X = -0.015$ m and the surface. Translational and internal temperatures decreased by a maximum of approximately 2000 and 1500 K, respectively, due to the high radiative energy in this region after one iteration of DSMC–PMC coupling. At this altitude, after the first iteration, the temperature profiles did not change significantly as additional coupling calculations were performed.

The convective and radiative heat fluxes to the vehicle surface were also calculated and compared for cases with and without radiation at 61.8 km in Fig. 13. The convective heat flux spatial distribution is similar to that at the higher altitude of 71.9 km, but, in

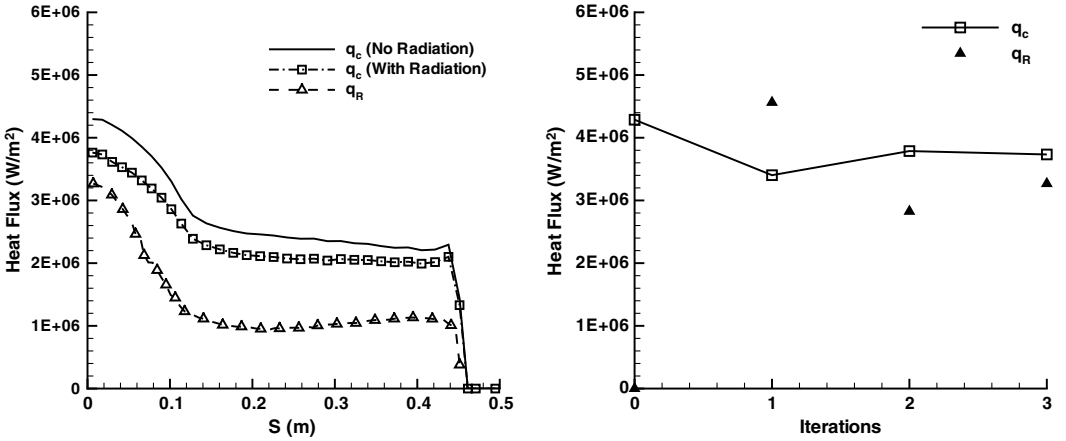

Fig. 13 Comparison of heat flux along the forebody surface for cases with and without radiation (LHS) and heat flux at the stagnation point as a function of DSMC–PMC coupling iterations (RHS) for the Stardust body at the 61.8-km altitude.

this case, the peak radiative heat flux is at the stagnation point. The radiative heat flux spatial dependence is consistent with the electron number density and temperature contours shown in Fig. 6, where both parameters are seen to have maximum values in the stagnation region only. It is also observed that the convective heat flux along the surface is reduced by the effect of radiation cooling. Figure 13 (RHS) presents the convective and radiative heat fluxes to the stagnation point with respect to the number of coupling iterations. The figure shows that both the convective and radiative heat fluxes are nearly converged after the first iteration. It can be seen that surface convective heat flux after the first coupling iteration decreases by 21% due to radiation. However, with further coupled iterations, the convective heat flux obtained from the third iteration is not significantly different from the second iteration result, and, finally, the convective heat flux after three iterations is reduced by 13%. The behavior in the change of the convective heat flux as a function of iteration at the stagnation point is also consistent with the small change in the translational temperature profiles shown by the LHS of Fig. 12. The contribution of the radiative heat flux to the total heat flux is approximately 46% at this altitude. Because there is no additional heat at the surface due to atomic recombination using the noncatalytic surface condition, the convective heating rate to the surface is not much higher than the radiative heating. Thus, the effect of radiative heating to the noncatalytic surface must be considered at the vehicle design stage.

In summary, the net effect of radiation on the flowfield temperatures and heat fluxes are similar at both the 71.9 and 61.8-km altitudes. However, the detailed convergence of the flow-radiation coupling is different. At the lower altitude, the radiative energy does not influence the distribution of energy modes in the gas because the flow is sufficiently dense to be closer to thermochemical equilibrium. This is consistent with the fact that the QSS solution for the electronic state populations is dominated by electron impact collisions. Thus, the temperatures and convective heat flux are not changed after even the first iteration. In contrast, at the higher altitude, it was found that flow noticeably changes after the first and second radiation coupling iterations, but the flow change is overestimated. Further iterations are required to obtain converged temperature and convective heat flux.

C. Uncertainty Estimation of Radiative Heat Flux due to the Statistical Deviation of Flow Properties in DSMC

Since the DSMC is a statistical particle method, the finite sample size (related to numbers of particles and collisions) will affect the uncertainty in the radiation predictions. The PMC approach for modeling the RTE is also a statistical approach, and its uncertainty levels are related to the number of photon bundles selected. The selection of the two different sets of numerical parameters for each method is completely independent, suggesting that we can estimate the total uncertainty in the radiative heat flux by taking the square root of the sum of the squares of the individual uncertainties in DSMC and PMC. The PMC simulations in this work used a number of photon bundles that generally corresponded to an uncertainty of 1% or less, as listed in the first row of Table 2. It will be seen that PMC uncertainties are smaller than those of DSMC so that the major contribution to the uncertainty in the radiative heat flux is due to the noise in DSMC samples, as inferred from the finite numbers of particles and cells listed in the last two rows of Table 1.

The most thorough analysis would use multiple DSMC flows based on the standard deviation of the different macroparameters as input to a number of separate PMC simulations. The average and standard deviation of the radiation computed using the PMC simulation would then illustrate the effect of the DSMC uncertainties on the PMC radiation calculation. Unfortunately, running the PMC over such a highly multidimensional parameter space would be difficult. For this reason, we made two reasonable approximations to make the assessment feasible. First, we used the much faster tangent slab approximation to the RTE, which is as accurate as the PMC at the stagnation point, the location where the uncertainty estimation is being performed. Then, we assumed that, in each cell along the stagnation streamline, the range in DSMC values of electron temperature and number density, the two macroparameters that are the important properties to compute radiation, could be represented by different normal distributions, each with a confidence level of 95%. Note that, when we repeated the entire analysis of the uncertainty in the stagnation point radiative heat flux, assuming a confidence level of 99% to define the macroparameter normal distribution functions, there was no significant difference in the mean and standard deviation of the stagnation point radiative heat flux. The neutral atomic number densities and translational temperature are also important factors for calculating radiation; however, the noise in these parameters is negligibly small and was neglected in this analysis. The statistical parameters of the mean value and the standard deviation of the electron number densities and temperatures were calculated using 30,000 sampling steps in each cell along the stagnation streamline. The minimum and maximum value of the ratio of the standard deviation to the mean value for the two macroparameters in the approximately 25 cells along the stagnation streamline are given for each altitude in the second and third row of Table 2. It can be seen that the ratios are largest for the higher altitude of 81 km, consistent with the smaller number of DSMC particles. The maximum uncertainty values presented in the second and third rows correspond to values in the freestream and therefore will have little effect on the radiation uncertainty because freestream emission is orders of magnitude lower than the peak values in the shock.

With the macroparameter distributions so prepared, we then sampled the electron number density and temperature values using the acceptance-rejection method [19], which is based on the assumption that flow properties follow a normal distribution function with a confidence level of 95%. For each sample, the stagnation point radiative heat flux was calculated using this flow-sampled data in the TS approximation. This procedure was repeated 1000 times, a value that was determined to be sufficient such that both the average and standard deviation values of the stagnation point radiative heat flux remained unchanged.

The uncertainties in the radiative heat flux to the stagnation point at each altitude are summarized in the fourth row of Table 2. It can be seen that the DSMC-TS uncertainty is higher than the pure uncertainty in the PMC method at all altitudes. Both the pure PMC and DSMC-TS uncertainties at 81 km are higher than those at the lower altitudes because the number of simulated particles and photon bundles used in that case was less than that for the lower altitudes, which in turn leads to the higher statistical variation in both DSMC and PMC. It can clearly be seen, however, that the total uncertainty in the DSMC-TS and PMC simulations is sufficiently small, such that the DSMC and the PMC predictions of the variation of the radiative

Table 2 Uncertainty in stagnation point radiative heat flux due to the statistical variation of DSMC flows

Parameter	61.8 km	65.4 km	71.9 km	81.0 km
PMC (%)	0.7	0.6	0.6	1.3
Min-max ratio for T_e (%)[a]	0.4–29.5	0.6–15.3	1.2–39.0	1.3–59.6
Min-max ratio for n_e (%)	0.8–34.8	2.3–16.1	2.6–29.1	2.5–34.4
DSMC—TS Analyses (%)	1.4	2.4	2.4	5.2
Total [(DSMC–TS Analyses^2 + PMC^2)$^{0.5}$, %]	1.6	2.5	2.5	5.4

[a]The minimum and maximum ratio of the standard deviation to the mean value found in the 25 cells (approximate number for each altitude) along the stagnation streamline are given.

heat flux with altitude are much greater than the statistical uncertainties. Hence, the coupled DSMC–PMC simulations can be used to understand the dependence of heat flux with altitude for a reentry trajectory, as will be discussed in the next subsection.

D. Discussion of Convective-Radiative Heating During the Stardust Reentry Trajectory

This section compares the stagnation point convective and radiative heat fluxes for the Stardust vehicle along the reentry trajectory obtained from the coupled DSMC/FV-PMC method with previous results. Figure 14 shows a comparison of convective heat flux to the stagnation point with and without radiation coupling as a function of the product of the square root of the freestream mass density and the freestream velocity raised to the cubic power. The latter is chosen for the abscissa of the figure based on the correlation of convective heat flux with freestream conditions suggested by Sutton [41] and discussed further in Anderson [42]. Also shown is a comparison of our DSMC results with the previous CFD calculations performed by Olynick et al. [1]. First it can be seen that both CFD and DSMC predict a linear dependence of convective heat flux on the freestream correlation. It can also be seen that the DSMC–PMC-coupled convective fluxes have a very similar dependence with altitude to the DSMC without radiation values. The difference in magnitudes between these two cases is small, but some decrease in the convective heat flux occurs when radiative cooling is taken into account. Both sets of results are consistent with the results presented earlier in Sec. V. The difference between the DSMC results and those of Olynick et al. [1] is a factor of 2 to 3 and is due to the use of the fully catalytic surface condition in the CFD simulations. This conclusion was validated by performing DSMC simulations with a catalytic surface condition using the implementation discussed in Sec. III. The DSMC simulations are not coupled with the PMC radiation; however, the effect of radiation coupling on the convective heat flux is much smaller than that of the gas-surface interaction model. Given the very different numerical approaches, the CFD and DSMC convective heat flux dependence with freestream conditions are believed to be in good agreement and the difference is within 20%.

The radiative heat flux to the stagnation point at the same four altitudes is shown in Fig. 15. In this figure, two PMC radiation results, which use Doppler and Voigt line shapes, are compared to Olynick's results and the radiative heat flux correlation suggested by Tauber and Sutton [43]. In the correlation of Tauber and Sutton [43], stagnation point radiative heating relations for Earth and Mars entries were developed using an equilibrium radiation model coupled with an inviscid flowfield code that assumed thermochemical equilibrium conditions. Their relationship [43] used tabulated radiative heating velocity functions and a linear interpolation to calculate the stagnation point radiative heating rate. The radiative heating is not quite linearly related to the freestream velocity and density. We

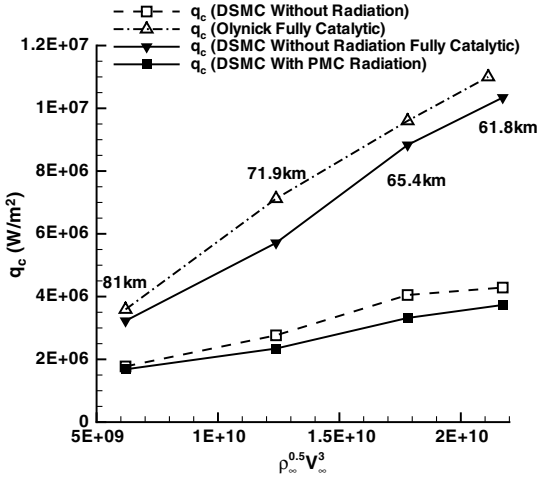

Fig. 14 Comparison of the stagnation point convective heat flux versus freestream correlation during the Stardust reentry trajectory.

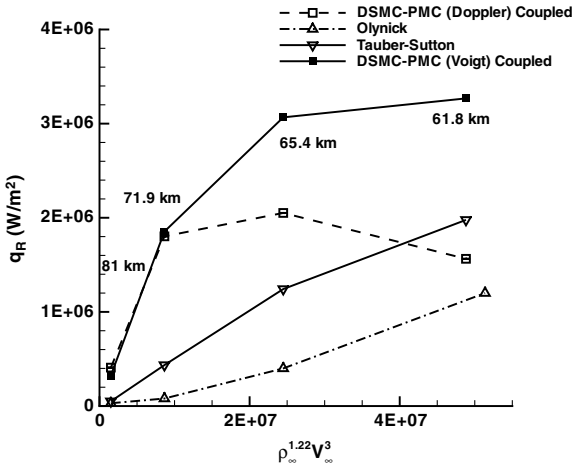

Fig. 15 Comparison of the stagnation point radiative heat flux versus freestream correlation during the Stardust reentry trajectory.

obtained a correlation of these results with $\rho_\infty^{1.22}V_\infty^3$ as our independent variable on the X axis of Fig. 15 by trial and error. The power of the freestream number density is given by the Tauber and Sutton correlation, but the freestream velocity power dependence was selected such that the radiative heat flux should vary linearly with it. The freestream correlation used previously to calculate the abscissa for the convective heat flux is used again in Fig. 15.

Two important conclusions can be drawn from Fig. 15, i.e., the DSMC, CFD, and Tauber–Sutton correlation have different magnitudes and altitude dependence. The agreement, however, between the CFD and the correlation is not better than the DSMC-CFD agreement because the flow and radiation models used in the correlation are different from those of Olynick's CFD calculation. In Tauber and Sutton's work, thermochemical equilibrium and nonablation are assumed throughout. The differences in flow modeling between the two continuum approaches also have a large influence on the radiative heating; and it has been shown by Hash et al. [13] that, even when different continuum flow models predict similar convective heating, the radiative heating rates can be significantly different.

With respect to the DSMC–PMC-coupled simulations, we see that using the Doppler line shape predicts a different freestream dependence compared to that obtained using the Voigt line shape. In addition, the stagnation point radiative heating calculated from the DSMC–PMC with the Doppler line shape is not linearly related to the freestream correlation. Since Doppler line broadening is only dependent on the translational temperature, the wings of the narrow atomic lines are not sufficiently broadened compared to the Voigt line shape so that the net radiatively transferred energy is almost reabsorbed near the line-center wavelength. However, for the high electron concentration flows discussed here, electron collisions are an important mechanism for line broadening. By using the Voigt line shape and the combination of Gaussian and Lorentzian line broadening components, the wings of a line extend further from the line-center, allowing the transport of strong spectral radiative flux in the line wings. When the Voigt line shape is used in DSMC–PMC coupling calculations, the peak radiative heating occurs near the 61.8-km altitude, and the stagnation point radiative heating rate is proportional to the freestream correlation, similar to the CFD results.

In addition, the question remains why the DSMC–PMC simulations that use the Voigt line shape predict a radiative heat flux about a factor of 2 higher than the CFD results of Olynick. Olynick's calculations used the NOVAR radiation model, which was developed from the LORAN code. This model calculates atomic line as well as continuum and molecular radiation using a one-dimensional TS approximation. However, differences in the radiation approaches used in the DSMC and CFD results presented here are not assessed to be the main reason for the discrepancies in the radiative heat flux. Our previous comparisons with CFD simulations for Stardust as well as the DSMC simulations of others find that the electron temperature in DSMC is predicted to be nearly twice as high as the internal

temperatures in continuum flow models [18,44]. Since the population of the upper electronic levels for strong atomic emitters is strongly dependent on the electron temperature, this discrepancy between the CFD and DSMC simulations has a significant impact on the radiative heat flux. This discrepancy could probably be reduced by using similar thermochemical models in the two different gas dynamic approaches [13] and should be strongly considered for reentry flows into highly nonequilibrium atmospheric conditions.

VI. Conclusions

Coupled DSMC flowfield FV-PMC radiation simulations were performed for the Stardust reentry trajectory from transitional to continuum peak heating conditions to examine the effect of radiation on high-Mach-number flows. This paper presents the first such simulations performed using the high-fidelity DSMC kinetic method. Building on previous Stardust modeling, the DSMC simulations employed a chemistry model that included ionization as well as high-energy relaxation models. To enable a direct comparison with CFD results at peak heating, a fully catalytic surface condition was implemented in the DSMC simulations. Using this surface boundary condition, the DSMC and CFD convective heat fluxes were found to be in good agreement within 20% difference, considering the very different gas dynamic approaches. A two-dimensional/axisymmetric version of the FV-PMC RTE method was implemented for direct use in the DSMC macroparameter sampling grid, using a photon weighting scheme that improves the photon bundle statistics along the axis of symmetry.

Using this newly developed approach, coupled DSMC-radiative transfer simulations were performed at four altitudes corresponding to a Stardust reentry trajectory. The flowfield internal energy was found to be reduced when coupled to the radiative transport, which in turn lowered the radiative heat flux. Convergence in the convective and radiative heat fluxes was typically obtained within three to four iterations. For the range of conditions considered, the radiative heat flux was found to be about 40% of the total heat flux, highlighting the nonequilibrium nature of the Stardust reentry flow. The DSMC results were found to more closely follow the Tauber–Sutton correlations for radiative heat transfer when the Voigt line shape was used. The differences in radiative heat flux obtained from the DSMC versus the CFD can be understood in terms of the different thermochemical models employed. Since the Tauber–Sutton correlations are based on CFD results, it is not surprising that they and the DSMC results do not have the same dependence on freestream parameters. For the nonequilibrium conditions of the Stardust reentry, these discrepancies are important and should be resolved.

Acknowledgments

The research performed at the Pennsylvania State University was supported by NASA through Grant No. NNX07AC47A. We would like to acknowledge M. Ivanov of the Institute of Theoretical and Applied Mechanics, Russia, for the use of the original SMILE code.

References

[1] Olynick, D., Chen, Y. K., and Tauber, M. E., "Aerothermodynamics of the Stardust Sample Return Capsule," *Journal of Spacecraft and Rockets*, Vol. 36, No. 3, 1999, pp. 442–462. doi:10.2514/2.3466

[2] Beerman, A. F., Lewis, M. J., Starkey, R. P., and Cybyk, B. Z., "Significance of Nonequilibrium Surface Interations in Stardust Return Capsule Ablation Modeling," *Journal of Thermophysics and Heat Transfer*, Vol. 23, No. 3, 2009, pp. 425–432. doi:10.2514/1.38863

[3] Johnson, E. J., Starkey, R. P., and Lewis, M. J., "Aerodynamic Stability of Reentry Heat Shield Shapes for a Crew Exploration Vehicle," *Journal of Spacecraft and Rockets*, Vol. 43, No. 4, 2006, pp. 721–730. doi:10.2514/1.20044

[4] Gupta, R. N., "Aerothermodynamic Analysis of Stardust Sample Return Capsule with Coupled Radiation and Ablation," *Journal of Spacecraft and Rockets*, Vol. 37, No. 4, 2000, pp. 507–514. doi:10.2514/2.3592

[5] Suzuki, T., Furudate, M., and Sawada, K., "Trajectory-Based Heating Analysis for the Stardust Sample Return Capsule," *40th AIAA Aerospace Sciences Meeting and Exhibit*, AIAA Paper 2002-0908, Reno, NV, Jan. 2002.

[6] Park, C., "Calculation of Stagnation-Point Heating Rates Associated with Stardust Vehicle," *Journal of Spacecraft and Rockets*, Vol. 44, No. 1, 2007, pp. 24–32. doi:10.2514/1.15745

[7] Liu, Y., Prabhu, D., Trumble, K., Saunders, D., and Jenniskens, P., "Radiation Modeling for the Reentry of the Stardust Sample Return Capsule," *46th AIAA Aerospace Sciences Meeting and Exhibit*, AIAA Paper 2008-1213, Reno, NV, Jan. 2008.

[8] Olynick, D. R., Henline, W. D., Chambers, L. H., and Candler, G. V., "Comparison of Coupled Radiative Flow Solutions with Project Fire II Flight Data," *Journal of Thermophysics and Heat Transfer*, Vol. 9, No. 4, 1995, pp. 586–594. doi:10.2514/3.712

[9] Hartung, L. C., "Development of a Nonequilibrium Radiative Heating Prediction Method for Coupled Flowfield Solutions," *Journal of Thermophysics and Heat Transfer*, Vol. 6, No. 6, 1992, pp. 618–625. doi:10.2514/3.11542

[10] Whiting, E. E., Park, C., Liu, Y., Arnold, J. O., and Paterson, J. A., "NEQAIR 96 User Manual," NASA RP-1389, 1996.

[11] Johnston, C. O., Hollis, B. R., and Sutton, K., "Radiative Heating Methodology for the Huygens Probe," *Journal of Spacecraft and Rockets*, Vol. 44, No. 5, 2007, pp. 993–1002. doi:10.2514/1.26424

[12] Wright, M., Candler, G. V., and Bose, D., "Data-Parallel Line Relaxation Method for the Navier-Stokes Equations," *AIAA Journal*, Vol. 36, No. 9, 1998, pp. 1603–1609. doi:10.2514/2.586

[13] Hash, D., Olejniczak, J., Wright, M., Prabhu, D., Pulsonetti, M., Hollis, B., Gnoffo, P., Barnhardt, M., Nompelis, I., and Candler, G., "Fire II Calculations for Hypersonic Nonequilibrium Aerothermodynamics Code Verification: DPLR, LAURA and US3D," *45th AIAA Aerospace Sciences Meeting and Exhibit*, AIAA Paper 2007-605, Reno, NV, Jan. 2007.

[14] Sohn, I., Bansal, A., Levin, D. A., and Modest, M. F., "Advanced Radiation Calculations of Hypersonic Reentry Flows Using Efficient Databasing Schemes," *Journal of Thermophysics and Heat Transfer*, Vol. 24, No. 3, July–Sept. 2010, pp. 623–637.

[15] Feldick, A. M., Modest, M. F., and Levin, D. A., "Closely Coupled Flowfield-Radiation Interactions For Flowfields Created during Hypersonic Reentry," *40th Thermophysics Conference*, AIAA Paper 2008-4104, Seattle, WA, June 2008.

[16] Feldick, A. M., Modest, M. F., Levin, D. A., Gnoffo, P., and Johnston, C. O., "Examination of Coupled Continuum Fluid Dynamics and Radiation in Hypersonic Simulations," *47th AIAA Aerospace Sciences Meeting Including the New Horizon Forum and Aerospace Exposition*, AIAA Paper 2009-475, Orlando, Florida, Jan. 2009.

[17] Modest, M. F., *Radiative Heat Transfer*, 2nd ed., Academic Press, New York, 2003.

[18] Ozawa, T., Nompelis, I., Levin, D. A., Barnhardt, M., and Candler, G. V., "Continuum Method Comparison of a High Altitude, Extreme-Mach-Number Reentry Flow," *Journal of Thermophysics and Heat Transfer*, Vol. 24, No. 2, April–June 2010, pp. 225–240. doi:10.2514/1.42624

[19] Bird, G. A., *Molecular Gas Dynamics and the Direct Simulation of Gas Flows*, Clarendon, Oxford, 1994.

[20] Ozawa, T., Zhong, J., and Levin, D. A., "Development of Kinetic-Based Energy Exchange Models for Non-Continuum, Ionized Hypersonic Flows," *Physics of Fluids*, Vol. 20, No. 4, 2008, pp. 046102. doi:10.1063/1.2907198

[21] Gallis, M. A., and Harvey, J. K., "Nonequilibrium Thermal Radiation from Air Shock Layers Modeled with Direct Simulation Monte Carlo," *Journal of Thermophysics and Heat Transfer*, Vol. 8, No. 4, 1994, pp. 765–772. doi:10.2514/3.610

[22] Gallis, M. A., and Harvey, J. K., "Atomic Species Radiation from Air Modeled with Direct Simulation Monte Carlo Method," *Journal of Thermophysics and Heat Transfer*, Vol. 9, No. 3, 1995, pp. 456–463. doi:10.2514/3.687

[23] Ozawa, T., Li, Z., Sohn, I., Levin, D. A., and Modest, M. F., "Modeling of Electronic Excitation and Radiation for Hypersonic Reentry Flows in DSMC," *48th AIAA Aerospace Sciences Meeting Including the New Horizon Forum and Aerospace Exposition*, AIAA Paper 2010-987, Orlando, FL, Jan. 2010.

[24] Modest, M. F., "The Monte Carlo Method Applied to Gases with

Spectral Line Structure," *Numerical Heat Transfer, Part B: Fundamentals*, Vol. 22, No. 3, 1992, pp. 273–284. doi:10.1080/10407799208944984

[25] Wang, A., and Modest, M. F., "Spectral Monte Carlo Models for Nongray Radiation Analyses in Inhomogeneous Participating Media," *International Journal of Heat and Mass Transfer*, Vol. 50, Nos. 19–20, 2007, pp. 3877–3889. doi:10.1016/j.ijheatmasstransfer.2007.02.018

[26] Wu, Y., Modest, M. F., and Haworth, D. C., "A High-Order Photon Monte Carlo Method for Radiative Transfer in Direct Numerical Simulation," *Journal of Computational Physics*, Vol. 223, No. 2, 2007, pp. 898–922. doi:10.1016/j.jcp.2006.10.014

[27] Ozawa, T., Wang, A., Levin, D., and Modest, M., "Development of Coupled Particle Hypersonic Flowfield—Photon Monte Carlo Radiation Methods," *Journal of Thermophysics and Heat Transfer*, Vol. 24, No. 3, July–Sept. 2010, pp. 612–622. doi:10.2514/1.44645

[28] Ozawa, T., Modest, M. F., and Levin, D. A., "Spectral Module for Photon Monte Carlo Calculations in Hypersonic Nonequilibrium Radiation," *Journal of Heat Transfer*, Vol. 132, No. 2, Feb. 2010, pp. 023406-1–023406-8.

[29] Feldick, A. M., Giegel, J., and Modest, M. F., "A Spectrally Accurate Tightly-Coupled 2-D Axisymmetric Photon Monte Carlo RTE Solver For Hypersonic Entry Flows," , American Society of Mechanical Engineers, Paper HT2009-88241, July 2009.

[30] Ivanov, M. S., Markelov, G. N., and Gimelshein, S. G., "Statistical Simulation of Reactive Rarefied Flows—Numerical Approach and Applications," *7th AIAA/ASME Joint Thermophysics and Heat Transfer Conference*, AIAA Paper 1998-2669, Albuquerque, NM, June 1998.

[31] Ivanov, M. S., and Rogasinsky, S. V., "Analysis of the Numerical Techniques of the Direct Simulation Monte Carlo Method in the Rarefied Gas Dynamics," *Soviet Journal of Numerical Analysis and Mathematical Modeling*, Vol. 3, No. 6, 1988, pp. 453–465. doi:10.1515/rnam.1988.3.6.453

[32] Bird, G. A., "Monte-Carlo Simulation in an Engineering Context," *Progress in Astronautics and Aeronautics*, Vol. 74, 1981, pp. 239–255.

[33] Borgnakke, C., and Larsen, P. S., "Statistical Collision Model for Monte Carlo Simulation of Polyatomic Gas Mixture," *Journal of Computational Physics*, Vol. 18, No. 4, 1975, pp. 405–420. doi:10.1016/0021-9991(75)90094-7

[34] Millikan, R. C., and White, D. R., "Systematics of Vibrational Relaxation," *Journal of Chemical Physics*, Vol. 39, No. 12, 1963, pp. 3209–3213. doi:10.1063/1.1734182

[35] Parker, J. G., "Rotational and Vibrational Relaxation in Diatomic Gases," *Physics of Fluids*, Vol. 2, No. 4, 1959, pp. 449–462. doi:10.1063/1.1724417

[36] Park, C., "Assessment of Two-Temperature Kinetic Model for Ionizing Air," *Journal of Thermophysics and Heat Transfer*, Vol. 3, No. 3, 1989, pp. 233–244. doi:10.2514/3.28771

[37] Park, C., *Nonequilibrium Hypersonic Aerothermodynamics*, Wiley, New York, 1990.

[38] Bird, G. A., "Nonequilibrium Radiation During Re-Entry at 10 km/s," *22nd AIAA Thermophysics Conference*, AIAA Paper 87-1543, Honolulu, HI, June 1987.

[39] Lee, J. H., "Electron-Impact Vibrational Relaxation in High-Temperature Nitrogen," *Journal of Thermophysics and Heat Transfer*, Vol. 7, No. 3, Sept. 1993, pp. 399–405. doi:10.2514/3.432

[40] Loeb, L. B., *Basic Processes of Gaseous Electronics*, University of California Press, Berkeley, CA, 1961.

[41] Sutton, K., "Air Radiation Revisited," *19th AIAA Thermophysics Conference*, AIAA Paper 84-1733, Snowmass, CO, June 1984.

[42] Anderson, J. D., *Hypersonic and High-Temperature Gas Dynamics*, 2nd ed., AIAA, Reston, VA, 2006.

[43] Tauber, M. E., and Sutton, K., "Stagnation-Point Radiative Heating Relations for Earth and Mars Entries," *Journal of Spacecraft and Rockets*, Vol. 28, No. 1, 1991, pp. 40–42. doi:10.2514/3.26206

[44] Boyd, I. D., Trumble, K., and Wright, M. J., "Nonequilibrium Particle and Continuum Analyses of Stardust Entry for Near-Continuum Conditions," *39th AIAA Thermophysics Conference*, AIAA Paper 2007-4543, Miami, FL, June 2007.